Ripple formation and smoothening on insulating surfaces

2009 J. Phys.: Condens. Matter 21 224005

(http://iopscience.iop.org/0953-8984/21/22/224005)

J. Phys.: Condens. Matter **21** (2009) 224005 (12pp) doi:10.1088/0953-8984/21/22/224005

Ripple formation and smoothening on insulating surfaces

Randall L Headrick[1] **and Hua Zhou**[2]

[1] Department of Physics and Materials Science Program, University of Vermont, Burlington, VT 05405, USA
[2] National Synchrotron Light Source, Brookhaven National Laboratory, Upton, NY 11973, USA

Received 28 January 2009
Published 12 May 2009
Online at stacks.iop.org/JPhysCM/21/224005

Abstract
Ion bombardment of insulating surfaces such as Al_2O_3 and SiO_2 produces ordered patterns of ripples. The ripple wavelength varies with ion energy, incidence angle and substrate temperature. A region of stability is also known to exist for near-normal incidence during Ar^+ ion bombardment, where initially rough surfaces are smoothened. A number of relaxation mechanisms are found to be operative under specific conditions, including: surface-confined viscous flow, impact-induced lateral currents and impact-assisted surface diffusion during ion bombardment at high temperatures. Most of the experimentally observed phenomena are explained through extension of the Bradley–Harper theory by the addition of these new processes. Phenomena that are not explained by the linear theory, such as the saturation of surface amplitude during the formation of ripples, are thought to arise from nonlinear effects. This contribution describes the present status of the linear theory relevant to this class of materials and recent experimental results.

1. Introduction

This paper reviews and extends recent results pertaining to the formation of ripple patterns on surfaces by ion bombardment and smoothening by ion bombardment. Ar^+ ions in the energy range 300 eV–2 keV were used for all of the main experiments that are discussed [1–3]. Other ion species such as H^+, He^+, Ne^+, Xe^+ and Ga^+ are also commonly used to bombard surfaces of similar materials [4–6], and significantly higher particle energies into the MeV range have been used in some studies [7]. The purpose of the work, and our primary interest in this paper, is to enable a description of roughening and smoothening processes on surfaces in terms of fundamental mechanisms occurring at the surface during ion erosion. Although the field is an interesting area of science in its own right, an understanding of fundamental processes is relevant to a number of practical areas: (i) there is significant interest in using self-organized patterning as an easy route for the production of large-area nanostructured surfaces [8]; (ii) ion etching is a common step in lithographic patterning, while roughening sets a limit on the uniformity of layers thus produced; (iii) depth profiling by ion bombardment depends on uniform erosion, whereas roughening leads to a loss of depth resolution; and (iv) certain thin film deposition processes employ energetic particles. For example, sputter deposition sources and pulsed laser plumes produce energetic particles that may have a positive or detrimental effect on the properties of films, depending on the exact conditions and the type of film being deposited. Thus, an improved understanding of the effects of energetic particles on surfaces may spur developments in all of these areas.

1.1. Scope of this contribution

1.1.1. Materials systems. The materials systems to be discussed include the simple oxides SiO_2 and Al_2O_3, while literature results for diamond are mentioned for comparison. The similar behavior of these materials is presumably related to common underlying physical mechanisms, and may also reflect certain material properties. For example, the surfaces of these materials maintain the stoichiometry of the substrate during ion bombardment [9], although a thin amorphous surface layer with reduced density is typically formed. Therefore, effects due to preferential sputtering are not expected to be dominant. Another relevant property is that these materials are not highly chemically reactive and, as such, are apparently not prone to effects due to trace amounts of surface contamination [10, 11]. On the other hand, Al_2O_3 remains crystalline during ion

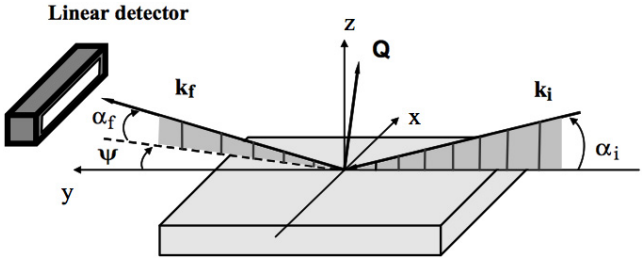

Figure 1. Geometry of the grazing incidence small-angle x-ray scattering experiment that is used for *in situ* measurement of the evolution of surface morphology. Reprinted with permission from [2]. Copyright 2007 by the American Physical Society.

bombardment at high temperatures (1000 K), which enables us to evaluate effects that may depend on the crystallinity of the surface.

1.1.2. Literature reviewed. Work in which the authors were directly involved over the last several years are discussed in detail. These include results on ripples formed on silicon dioxide surfaces by Ar^+ sputtering [1], as well as rippling of sapphire and the transition between stable and unstable regimes as the angle of incidence is varied [2, 3]. In addition, substantial experimental agreement with these results is evident in results found in the literature for other insulating systems, including diamond and quartz [4, 12]. Theoretical models extend the model of Sigmund, and of Bradley and Harper [13, 14].

1.1.3. Extensions of previous results. Since ion-smoothened surfaces may exhibit root-mean-square roughness values of 0.1 nm or less, characterization of their power spectral density (PSD) is complicated by the presence of correlated and uncorrelated noise in the image, which originates in the AFM instrument. A procedure for analysis of atomic force microscope images by subtraction of this noise is described. The results of this analysis are consistent with the results of x-ray scattering.

2. Experimental methods

2.1. Synchrotron x-ray scattering

Synchrotron x-ray scattering is a powerful and flexible method of analyzing surface morphology in real time. It is intrinsically a nanoscale probe, capable of resolving surface features from atomic dimensions to microns with sub-monolayer sensitivity, and sub-second temporal resolution due to the small x-ray wavelength ($\lambda \approx 0.12$ nm), and the very high brightness of modern synchrotron sources. Surface roughness can be characterized quantitatively. For example, if a model for the correlation function of surface roughness exists, then the distorted wave Born approximation (DWBA) may be used to compute the corresponding diffuse scattering profile [15, 16]. Alternately, the first-order perturbation theory (PT) may be used to relate the power spectral density (PSD) of surface roughness directly to the scattering pattern [17, 18]. The

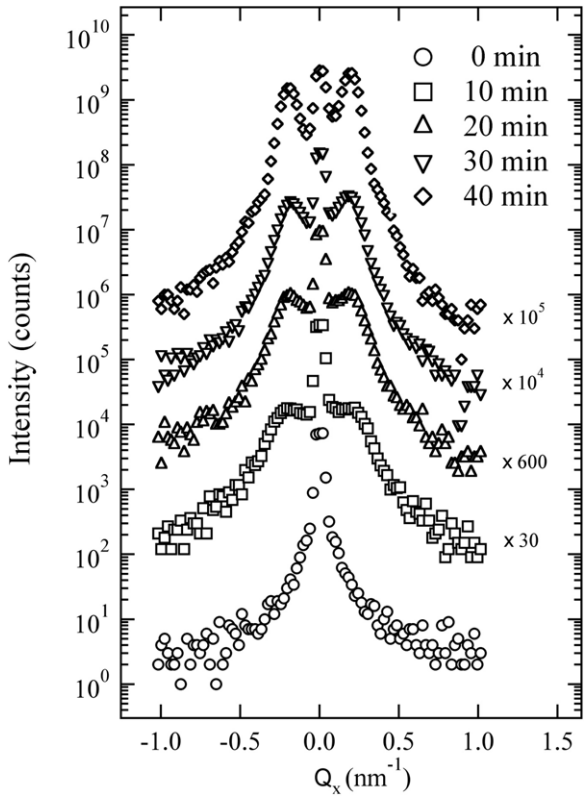

Figure 2. GISAXS spectra during formation of ripples on sapphire by Ar^+ at 500 eV and 45° incidence. The ion flux was $\approx 10^{15}$ ions cm^{-2} s^{-1}.

grazing incidence small-angle x-ray scattering (GISAXS) method does not rely on diffraction and therefore does not require a crystalline material [19]. However, grazing incidence x-ray diffraction (GIXD) is a related method that can be used to extract structural information from crystalline surfaces, and has been used, for example, in studies of surface structure [20–22], phase transitions [23, 24] and the evolution of surface morphology during crystal growth [25, 26]. GISAXS has been employed for numerous measurements of both crystalline and amorphous surfaces, including measurement of nanoparticles on surfaces [19], coarsening behavior during ion erosion [27] and measurement of the PSD of a surface during film deposition [28] or ion erosion [29].

The measurements discussed here and previously reported in [1] were performed at the A2 station of the Cornell High Energy Synchrotron Source. Later measurements were performed at the X21 facility for *in situ* analysis of film growth and processing at the National Synchrotron Light Source (NSLS) [2, 3]. Typical measurements employ GISAXS in the geometry depicted in figure 1. The incidence angle α_i and exit angle α_f may be varied in order to vary the magnitude of the scattering vector $\vec{Q} = \vec{k}_f - \vec{k}_i$ along the z axis. In the GISAXS geometry, the incidence and exit angles of the x-rays are usually adjusted to be near the critical angle for total external reflection (0.2° for 10 keV x-rays incident on sapphire). We detect scattering at different ψ in order to map Q_x. Figure 2 shows an example of the evolution of the GISAXS signal from a sapphire surface during 500 eV Ar^+ bombardment.

Early versions of the experiment used an NaI scintillator point detector and required a scan of the angle ψ. However, more recently we have employed a 384-pixel linear detector which allows the capability to characterize surface morphology in real time with high temporal resolution. In terms of scattering momentum transfer, the linear position-sensitive detector acquires all signals in one scan over a range of Q_x at constant Q_z and Q_y (typically $Q_z \leqslant 1$ nm^{-1}, $Q_y \approx 10^{-3}$ nm^{-1}, and Q_x varies over the range ± 1 nm^{-1}). This 'in-plane' scattering geometry allows maps of surface scattering to be measured, which can be approximately understood as maps of the PSD of the surface.

2.2. Ion bombardment

Ar^+ ions are produced by a high flux source ($J_{\text{ion}} \approx 10^{15}$ ions cm^{-2} s^{-1}) in the energy range 300–1000 eV, or by a low flux sputter gun ($J_{\text{ion}} \approx 10^{13}$ ions cm^{-2} s^{-1}) in the range 500–2000 eV. The base vacuum in the processing chamber is typically 10^{-9} Torr. A four-grid 3 cm ion source (Ion Tech) was used as the etching source for the experiment depicted in figure 2. The four-grid source is equipped with an electron source to neutralize the beam, which helps to prevent charging of insulating surfaces. The incidence angle of the ion beam is varied by rotation of the sample about an axis passing through the sample surface by a high precision stage.

The widely different densities provide a way to check for flux dependence of the results. Since no flux dependence of the ripple wavelength has been observed for either sapphire or silicon dioxide substrates, we will not discuss this parameter at length, except to point out that certain models of ripple formation predict that the ripple wavelength does depend on the ion flux and are therefore inconsistent with recent experiments. We note that it is essential to perform cross-checks between the gridded source and the grid-less source because gridded ion sources can introduce trace contamination, which can dramatically alter the results for some material systems [10, 11, 30]. These effects can be mitigated somewhat by monitoring the ion current on the final grid and minimizing it by adjusting the accelerator grid voltage. Cross-checks for sapphire and silicon dioxide substrates using a four-grid source versus a Phi sputter gun have so far yielded identical results. Beam divergence (typically 2°) may also increase if the accelerator grid voltage is not optimized [31].

2.3. Atomic force microscopy

Ex situ AFM is used to confirm the ripple wavelength and as a way to image morphology in real space. PSD curves produced from AFM data can also be used to study the distribution of roughness as a function of surface wavenumber. Since smoothened surfaces are isotropic, the circularly averaged PSDs can be examined, which often exhibit power law behavior that is characteristic of the smoothening mechanisms. Measurements reported in this paper were performed with a Digital Instruments Nanoscope-E Microscope in contact mode. Several results were subsequently rechecked using a Nanoscope-III operating in tapping mode.

3. Roughening and smoothening phenomena

In this section, the basic phenomena observed during Ar^+ in bombardment of insulating surfaces are introduced. Ripple patterns are normally formed for off-normal incidence near 45°. The AFM images in figure 3 show ripple patterns formed on (a) sapphire and (b) thermal SiO_2. Smoothening of initially roughened surfaces occurs during ion bombardment at normal incidence, as shown in figures 3(c) and (d) for sapphire and silicon dioxide, respectively. The effects are highly reproducible, independent of ion flux, and the ripple wavelength does not change with etching time. Normal incidence smoothening to root-mean-square amplitudes of ≈0.1 nm is routinely achievable. Figure 4 shows the effect of ion beam smoothening on the GISAXS intensity as a function of Q_x. Another effect is the formation of a thin amorphous layer created by ion bombardment with a thickness determined by the ion penetration depth. This layer has a reduced density and may be observed using either x-ray reflectivity [32] or cross-sectional transmission electron microscopy [5].

4. Theoretical methods

4.1. Sigmund theory of sputtering

In the Sigmund theory, erosion is modeled as arising from energy deposited into recoil atoms in a region around the track of each incident ion [13]. A Gaussian distribution of the deposited energy is assumed, as illustrated in figure 5. The expression for the energy density $E(\vec{r})$ produced by an ion with initial energy ϵ is taken to be

$$E(\vec{r}) = \frac{\epsilon}{(2\pi)^{3/2}\sigma\mu^2} \exp(-(Z-a)^2/\sigma^2 - (X^2+Y^2)/\mu^2) \quad (1)$$

where Z is the distance along the path of the ion track relative to the point where the ion enters the surface, while X and Y are the lateral distances perpendicular to the ion track. The parameters σ and μ represent the widths of the energy density and a is the ion range, as depicted in figure 5. The values of the parameters a, σ, μ can be estimated by simulations using the SRIM program [33].

The erosion rate is assumed to be proportional to the energy density at the surface, which varies with the surface morphology. In particular, valleys are eroded faster, since they intersect, on average, a higher energy density than do hillocks. The erosion rate v_0, and higher-order terms such as the coefficients ν_x, ν_y that describe corrections to the erosion rate when the surface has a curvature, can be determined quantitatively [34, 14]. The 'curvature-dependent erosion' effect is the key phenomenon on which all models of surface patterning during ion erosion are based, as described in the next section. Figure 6 shows the angle dependence of v_0 for Ar^+ erosion of sapphire.

4.2. Bradley–Harper theory

The height evolution of an ion-beam-eroded surface is described in the linear theory by a Langevin equation including

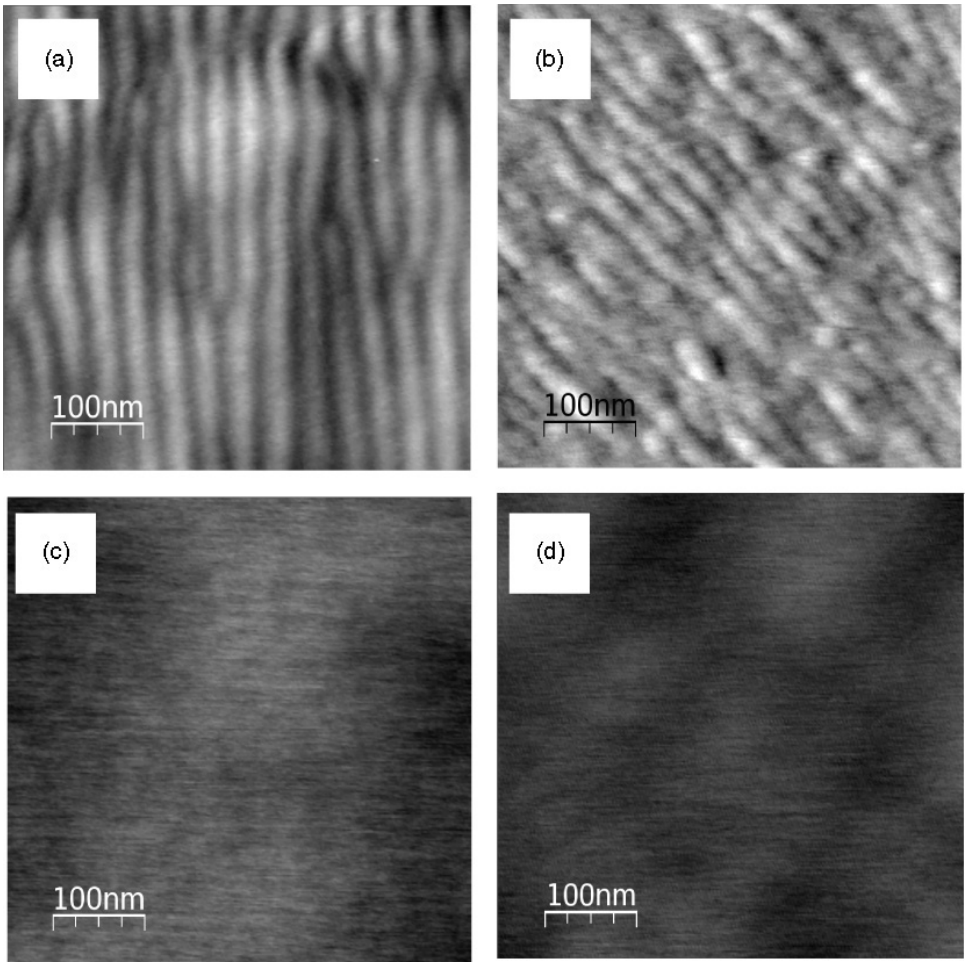

Figure 3. Atomic force microscope images for ripples produced on (a) sapphire for 600 eV Ar^+ bombardment at 45° and (b) silicon dioxide for 400 eV Ar^+ bombardment at 45°. Images of the same surfaces after ion smoothening are shown for (c) sapphire and (d) silicon dioxide. The root-mean-square amplitude of the images are 0.3, 0.2, 0.1 and 0.1 nm, respectively.

ion-induced roughening and surface smoothening:

$$\frac{\partial h(\vec{r},t)}{\partial t} = -v_0 + \nu_x \partial_{xx} h(\vec{r},t) + \nu_y \partial_{yy} h(\vec{r},t) - K\nabla^4 h(\vec{r},t) + \eta(\vec{r},t), \tag{2a}$$

$$\langle \eta(\vec{r},t)\rangle = 0, \qquad \langle \eta(\vec{r},t)\eta(\vec{r'},t')\rangle = v_0 \Omega \delta(\vec{r}-\vec{r'})\delta(t-t') \tag{2b}$$

where v_0, ν_x and ν_y are the average velocity and the curvature-dependent sputtering terms from Sigmund's theory [14, 34]. $\eta(x,t)$ is a Gaussian white noise term representing random fluctuations, uncorrelated in space and time, in the flux (J_{ion}) of the incoming ions. If we also take Ω as the substrate atomic volume and Y as the sputtering yield, then the relation $v_0 = Y\Omega J_{\text{ion}}\cos(\theta)$ connects the average erosion rate to the other terms. The factor $\cos(\theta)$ is present because J_{ion} is defined relative to the ion beam, while v_0 is defined relative to the surface. The leading term in equation (2*a*) can be neglected; then the surface height h is in a coordinate system that moves with the average surface during the erosion process. Bradley and Harper (BH) envisioned the coefficient K to represent surface diffusion or possible impact-induced surface diffusion; both effects are discussed in the next section. In BH, the coefficients ν_x and ν_y represent the curvature-dependent roughening or smoothening terms, which is a roughening term when it is negative but which becomes positive (stabilizing) at large angles of incidence (figure 7). However, the main smoothening mechanism is taken to be surface diffusion, which is introduced via the $\nabla^4 h$ term in equation (2*a*) and K is taken to be the surface diffusion coefficient. Note that other surface smoothening mechanisms, such as surface-confined viscous flow, will also produce a $\nabla^4 h$ term, which can modify the roughening/smoothening behavior, and will be discussed in a later section.

The structure factor $S(q,t)$ is obtained through a spatial Fourier transform of equation (2*a*) with the result

$$S(\vec{q},t) = \langle h(-\vec{q},t)h(\vec{q},t)\rangle = |h(q,0)|^2 e^{-2b(\vec{q})t} + \frac{v_0\Omega}{2b(\vec{q})}(1-e^{-2b(\vec{q})t}) \tag{3a}$$

$$b(\vec{q}) = \nu_x q_x^2 + \nu_y q_y^2 + K(q_x^2+q_y^2)^2. \tag{3b}$$

where $h(\vec{q},t)$ is the Fourier transform of surface height and $q = \sqrt{q_x^2+q_y^2}$ is the wavenumber of a particular surface mode [35, 36]. The function $b(\vec{q})$ includes terms representing the curvature-dependent erosion instability as well as all

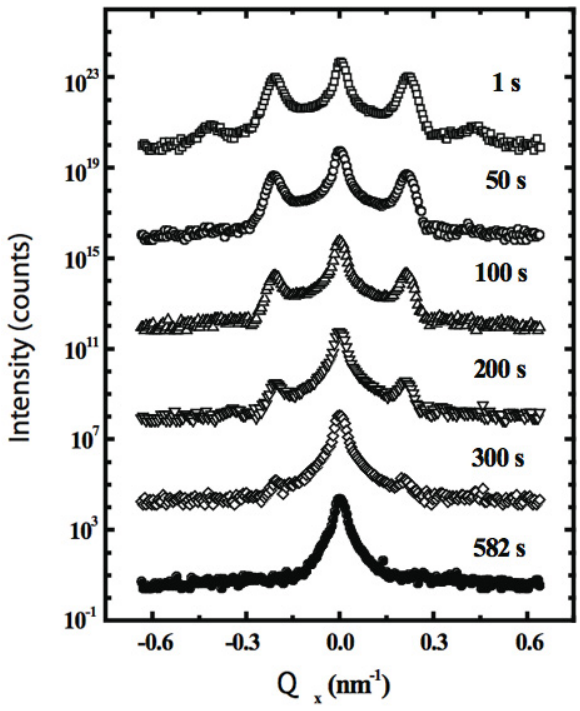

Figure 4. Smoothening of pre-patterned sapphire with normal incidence Ar^+ at 300 eV. The ion flux was $\approx 10^{15}$ ions cm^{-2} s^{-1}.

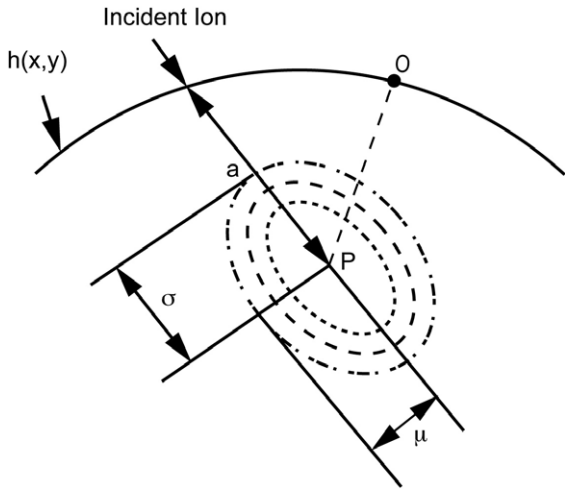

Figure 5. Schematic of the energy deposition inside the surface during the impact of a single ion. The point P represents the center of the energy deposition distribution, while point O represents a point on the surface at which the energy density is to be calculated.

operative mass transport mechanisms induced by ion erosion on the surface.

Ion smoothening of an initially rough surface can occur when $b(q)$ is positive for all q. Then the first term on the right-hand side of equation (3*a*) dominates the evolution of the PSD. Ion smoothening experiments are described in section 6. During pattern formation, one of the modes related to v_x or v_y often dominates the spectrum, and the PSD is reduced to a 1D pattern with a single dominant wavelength. Also, the first term of equation (3*a*) is a transient that becomes negligible if

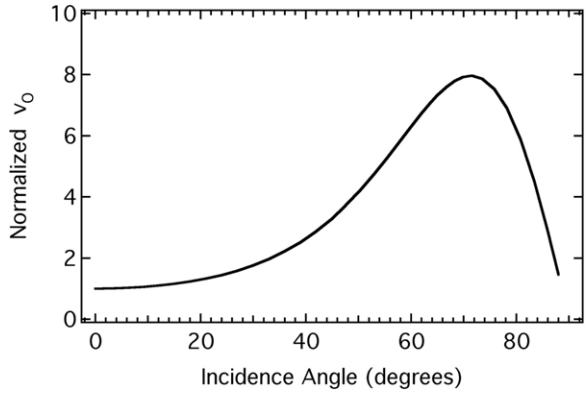

Figure 6. Calculated mean erosion velocity for 600 eV Ar^+ erosion of Al_2O_3. Parameters used were $a = 1.6$ nm, $\sigma = 0.6$ nm and $\mu = 0.5$ nm.

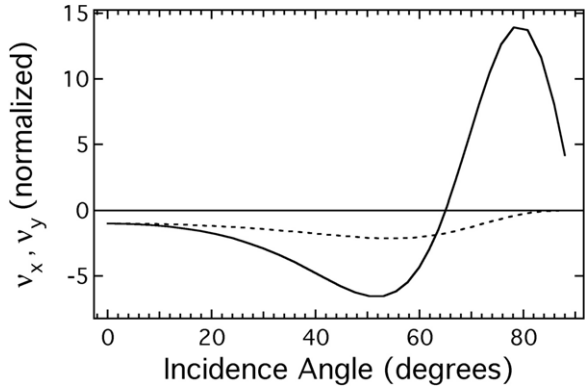

Figure 7. Plot of v_x (solid line) and v_y (dashed line) for Ar^+ bombardment of sapphire at 600 eV. Parameters used were $a = 1.6$ nm, $\sigma = 0.6$ nm and $\mu = 0.5$ nm.

the duration of the ion bombardment is long enough. Taking $h(q, 0) = 0$ and $|v_x| \gg |v_y|$, equations (3*a*) and (3*b*) become

$$S(\vec{q}, t) = v_0 \Omega \frac{(1 - e^{-2b(\vec{q})t})}{2b(\vec{q})} \tag{4a}$$

$$b(\vec{q}) = v_x q_x^2 + K(q_x^2 + q_y^2)^2. \tag{4b}$$

This expression is useful for analysis of the ripple formation instability. The essential feature of this equation that leads to surface instability and roughening is that $S(q)$ grows exponentially at any q where $b(q) < 0$, according to equation (4*a*). However, experimental observations show that the exponential growth occurs at early times only, while later the amplitude saturates due to nonlinear terms (see section 4.3.5). Also, note that the detailed shape of the curve given by equation (4*a*) does not give an accurate description of the roughness spectrum, which is an aspect of the problem that is not discussed in detail in this contribution.

The x direction is normally taken to be parallel to the projected ion beam direction along the surface, and the parallel mode is the one which has its wavevector along this direction, while the perpendicular mode has its wavevector in the y direction. The wavelength of ion sputtered ripples with

orthogonal orientations ℓ_x (parallel) and ℓ_y (perpendicular) are generally expressed as

$$\ell_x = 2\pi\sqrt{\frac{2K}{|\nu_x|}}, \qquad \nu_x < 0 \tag{5a}$$

$$\ell_y = 2\pi\sqrt{\frac{2K}{|\nu_y|}}, \qquad \nu_y < 0. \tag{5b}$$

The minimum between ℓ_x and ℓ_y determines which orientation dominates the ion-induced ripple topography.

The predictions of the model can be compared to experimental observations. Surface diffusion is independent of J_{ion}, but ν is proportional to J_{ion}, so that $\ell \propto J^{-1/2}$. We have not observed the ripple wavelength to be flux-dependent. Therefore, other mechanisms besides thermally activated surface diffusion have to be considered [1]. In addition, for surface diffusion, relaxation would occur even when ion bombardment has ceased. Since many of our structures are formed at room temperature this would imply that the surfaces would spontaneously smoothen after the ion bombardment has been turned off. In fact, nanostructures formed on simple oxide surfaces are stable in vacuum or air for months or even years. This suggests that, at low temperature, simple surface diffusion cannot be a relevant smoothening mechanism. Furthermore, we find that ion bombardment is required to produce smoothening, even at relatively high temperatures (1000 K) so that if surface diffusion is a relevant smoothening mechanism, then it must be of a type that is induced by ion bombardment. Impact-induced surface diffusion can explain the lack of ion flux dependence of the ripple wavelength, since $K_{\text{SD}} \propto J_{\text{ion}}$ and therefore equation (5) predicts a flux-independent ripple wavelength. Predictions for the ion energy dependence of the ripple wavelength can be tested to determine if impact-induced surface diffusion is the operative relaxation mechanism.

4.3. Extensions of Bradley–Harper theory

4.3.1. Surface-confined viscous flow. The ion-enhanced viscous flow relaxation (IVF) mechanism occurs by surface-confined viscous flow driven by surface tension. It can be the dominant smoothening mechanism for any material with an amorphous surface layer with reduced viscosity relative to the bulk value [1]. In this model, the surface diffusion coefficient K is replaced by the viscous relaxation rate $F_s d^3$, where d is the thickness of the relaxing layer so that

$$\ell_x = 2\pi\sqrt{\frac{2F_s d^3}{|\nu_x|}}, \qquad \nu_x < 0 \tag{6}$$

where F_s is proportional to γ/η_s, γ is the surface tension and η_s is the viscosity of a thin surface layer which has a viscosity lower than the bulk value because of ion irradiation [1, 6]. Since $F_s \propto J_{\text{ion}}$ it cancels the flux dependence of ν, and hence ℓ is independent of J_{ion}. The ion energy dependence of ℓ is given by the expression ϵ^p. A value of p between 0.67 and 0.77 is predicted if IVF is the main surface relaxation mechanism.

Temperature dependence is introduced through the assumption that the viscosity of the surface layer is reduced at high temperatures [1]. Then, $\ell_{\text{IVF}}(\epsilon, T) = H(\epsilon)W(T)$, where $H(\epsilon) = c\epsilon^p$ and the temperature-dependent factor $W(T) = \omega^{-1/2}[\exp(-\Delta E/k_B T) + \omega]^{1/2}$. The coefficients c give the wavelength at 1 keV, while ω determines the effect of the temperature-dependent part of the expression relative to the temperature-independent part. However, as we will see below for Ar^+ ion bombardment of sapphire, impact-induced surface diffusion may be a reasonable alternative mechanism to explain the behavior at high temperature.

4.3.2. Ion-assisted surface diffusion. Umbach *et al* discuss two variations of impact-induced surface diffusion [1]. Both models predict an exponent of $p = -0.55$ for the ion energy dependence. Both models also predict flux-independent wavelengths, as discussed in section 4.2.

4.3.3. Impact-induced lateral currents. The impact-induced lateral current (ILC) mechanism [42] is a 'fast' mechanism since it is related to recoils within the displacement cascade produced by individual ions. If the ion is incident off-normal relative to the local surface, then there will be a net displacement along the surface, which can be described mathematically as a current [45]:

$$\vec{j}_{\text{rec}} = -\frac{\nu_{\text{ILC}}}{\Omega}\nabla h, \tag{7a}$$

$$\frac{\partial h}{\partial t} + \Omega\nabla\cdot\vec{j}_{\text{rec}} = 0. \tag{7b}$$

On a rough surface the effect depends on the local slope, leading to an effective downhill current, and thus a smoothening effect.

The magnitude of the impact-induced lateral current (ILC) smoothening effect can be obtained from an analysis of the surface collision dynamics [45]. Zhou *et al* [3] have performed binary collision approximation (BCA) based *Monte Carlo* simulations of ion–matter collisions [33] in order to compute collision cascade induced displacements $\vec{d}_I$ ($I = 1, 2, \ldots, S$) for each recoil atom at and beneath the surface. The quantity S is the total number of recoil atoms for N incident ions. The lateral displacement of recoil atoms per incident ion can be represented as $\delta_{\text{rec},x} = (\sum_I d_{I,x})/N$ [45]. The ILC coefficient $\nu_{\text{ILC},x}$ is evaluated to be $(\Omega J_{\text{ion}}\cos(\theta))\partial\delta_{\text{rec},x}/\partial\theta$. Also, the expression for $\nu_{\text{ILC},y}$ is $(\Omega J_{\text{ion}}\cos(\theta))\delta_{\text{rec},z}$. Note that all parameters in the ILC computation are either known quantities or are readily obtained from the *Monte Carlo* simulations with reasonable accuracy.

If we assume that the average recoil vector $\vec{\delta}_{\text{rec}}$ is directed along the incident beam direction and that it has a constant magnitude, then we have $\delta_{\text{rec},x} \propto \sin(\theta)$ and $\delta_{\text{rec},z} \propto \cos(\theta)$. Both $\nu_{\text{ILC},x}$ and $\nu_{\text{ILC},y}$ are then proportional to $\cos^2(\theta)$. Figure 8 shows that the SRIM-calculated incidence-angle dependence does follow this law, with some deviation at larger angles.

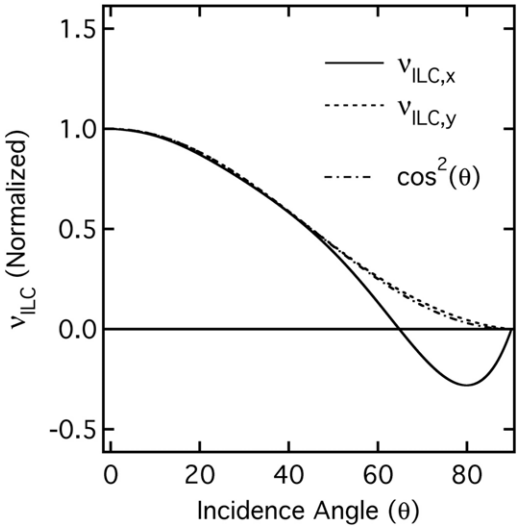

Figure 8. The impact-induced lateral current coefficients $\nu_{\mathrm{ILC},x}$ and $\nu_{\mathrm{ILC},y}$ obtained through SRIM simulations. Both coefficients are approximately proportional to $\cos^2(\theta)$.

4.3.4. Other linear terms. There are a variety of other linear mechanisms that could be considered. For example, biaxial stress can produce a surface instability [41]. Also, a nonlocal damping term has been proposed in order to explain patterns formed on semiconductor surfaces [43]. Various mechanisms are listed in table 1.

4.3.5. Nonlinear effects. Terms of the type $\lambda_x(\partial_x h)^2$ and $\lambda_y(\partial_y h)^2$ can be added to equation (2*a*) so that it becomes a noisy version of the Kuramoto–Sivashinsky equation. Park *et al* have studied this equation and have found that the system initially evolves according to the linear equation, but after a certain time the surface width saturates and the ripples gradually disappear [46]. For the cases discussed here, λ_x and λ_y are less than zero over most of the conditions studied. Under the condition $\lambda_x\lambda_y > 0$, gradual roughening according to a power law is expected.

Experimentally, sapphire and SiO_2 exhibit saturation of the ripple amplitude. However, no disappearance of the ripples are observed, or at least it occurs so slowly that it is not noticeable up to fluences of $\approx 10^{19}$ cm^{-2}.

5. Ripple formation experiments

Experiments aimed at determining the dependence of ripple wavelength on several parameters have been performed. In these experiments, samples are prepared using different ion energies or sample temperature, and the ripple wavelength is determined after ion bombardment by GISAXS or AFM. A wavelength versus phase angle diagram can also be constructed in which not only the wavelength, but also whether the ripples are present or absent is recorded. Also, the orientation of the ripples may be either parallel or perpendicular to the projection of the ion beam direction along the surface. The dependences on energy, temperature and angle are then compared with the predictions of models based on specific physical mechanisms in a linear theory that extends the BH theory. In each case, the roughening mechanism is taken to be curvature-dependent erosion driven by uncorrelated noise.

Table 1. Physical mechanisms of roughening and smoothening during ion erosion. In addition to these mechanisms, noise in the deposition process also significantly affects the roughness spectrum. Non-Gaussian erosion response functions have also been suggested to have a possible stabilizing effect [44].

Description	Stab./destab.	q-depend.
Surface diffusion [37, 38]	S	q^4
Surface conf. viscous flow [1, 39]	S	q^4
Surface erosion smoothening [40, 34]	S	q^4
Biaxial stress [41]	D	q^3
Impact ind. lateral current [42]	S	q^2
Curvature dep't erosion [13]	D[a]	q^2
Bulk viscous flow [37]	S	q^1
Nonlocal damping [43]	S	q^0

[a] Curvature-dependent erosion becomes stabilizing along the x direction at large angles of incidence, typically $\theta > 70°$.

5.1. SiO_2

Umbach *et al* studied the wavelength of parallel-oriented ripples formed by Ar^+ ion bombardment at 45°. The study evaluated the wavelength as a function of ion energy and sample temperature, and found that there is a temperature-independent part at low temperatures with an energy dependence ϵ^p, $p = 0.85$, which is consistent with ion-induced surface-confined viscous flow (predicted $p = 0.77$). On the other hand, the effective smoothening model [34] based on higher-order terms is not consistent with the data since it predicts wavelengths about one order of magnitude smaller than observed by experiments. At high temperatures, the wavelength becomes temperature-dependent. The energy-dependent factor $H(\epsilon)$ and the temperature-dependent factor $W(T)$ are shown in figure 9.

5.2. Sapphire

Zhou *et al* studied ripple formation on Al_2O_3 at two temperatures: 300 K, where the surface becomes amorphized, and 1000 K, where Reflection High Energy Electron Diffraction (RHEED) shows that the surface remains crystalline during ion bombardment [47]. At the lower temperature, the ion energy dependence of the ripple wavelength yields an exponent of $p = 0.71$, which is consistent with the IVF mechanism, and is also in agreement with the energy dependence obtained for SiO_2 by Umbach *et al* [1]. However, during ion bombardment at 1000 K, the exponent becomes $p = -0.44$. This significant change of the exponent signals a change in the relaxation mechanism to one which is nearly ion-energy-independent. Since the surface is crystalline at 1000 K, it is natural to conclude that surface diffusion is the dominant relaxation mechanism at this temperature, although it must be a type of surface diffusion that is stimulated by ion impact. A detailed mechanism for this impact-induced surface diffusion has not been proposed, but would likely involve aspects of models

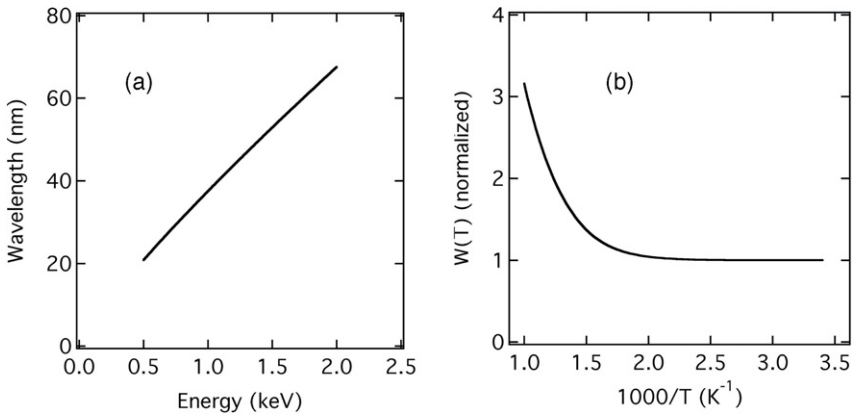

Figure 9. Ripple wavelength versus ϵ and T for Ar^+ bombardment of SiO_2. The curve in (a) gives the low-temperature behavior, while (b) represents a temperature-dependent factor that is independent of the ion energy. $H(\epsilon)$ represents the energy dependence of wavelength at low temperature, while $W(T)$ is the temperature-dependent factor normalized to the low-temperature value. The coefficients $c = 37.5$ nm, $\Delta E = 0.4$ eV and $p = 0.85$ were extracted from a fit to the data in [1].

involving impact-induced surface species [48] or diffusion within a thin ion-damaged surface layer [49]. Note that Umbach *et al* determined that $p = -0.55$ for several similar models. Zhou *et al* modeled the mechanism as being a temperature-dependent surface-diffusion-like term, so that the expression for the coefficient K is modified to

$$K(\epsilon, \theta, T) = K_{\mathrm{IVF}}(\epsilon, \theta) + K_{\mathrm{SD}}(T), \tag{8}$$

where the temperature dependence of the K_{SD} term is taken to be $\exp(-\Delta E_{\mathrm{SD}}/k_{\mathrm{B}}T)/T$. Figure 10 shows the prediction of this model for temperatures of 300 and 1000 K, with the activation energy $\Delta E_{\mathrm{SD}} = 0.72$ eV. The agreement is good over the region in which the experimental ripple wavelength is temperature-dependent.

Figure 10 shows that the ripple wavelength increases rapidly and becomes independent of temperature at low angles. Also, in the region below 25° ion incidence the surface does not form ripples at all. In fact, figure 4 shows that in this region a rough surface is actually smoothened. These observations suggest that an additional non-thermal mechanism becomes dominant for low angles of incidence.

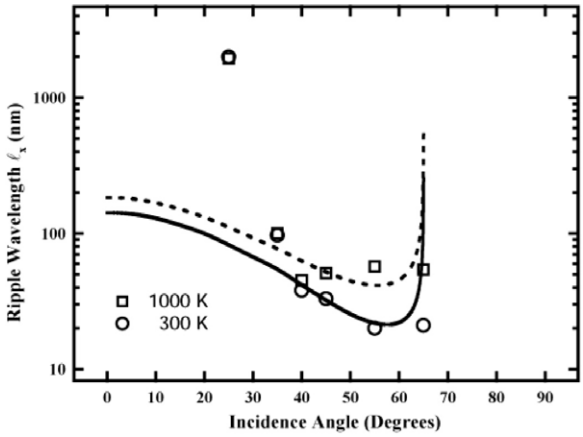

Figure 10. Sapphire wavelength vs angle for Ar^+ ion bombardment at 600 eV at two temperatures. At low temperature (300 K), the surface becomes amorphous during ion bombardment, while the surface remains crystalline at high temperature (1000 K). At 300 K, the surface is amorphized by ion bombardment, while at 1000 K the surface remains crystalline. The solid and dashed lines are calculated from equations (5*a*) and (8) for temperatures of 300 K and 1000 K, respectively, with $\Delta E_{\mathrm{SD}} = 0.72$ eV. The model fails to explain the temperature-independent data at 25° and 35°, and also the smooth region at lower angles. Note that the ripple direction is rotated for incidence angles above 65°, but these data points have been omitted from the plot. Reprinted with permission from [2]. Copyright 2007 by the American Physical Society.

6. Surface smoothening experiments

Under certain conditions, ions smoothen the surface rather than roughen it. These so-called 'windows of stability' are observed for several material systems when the angle of incidence is varied, and have attracted some attention recently [5, 44]. In our experiments, we start with a patterned surface with a ripple wavenumber q^* selected by choosing an appropriate angle of incidence using the data of figure 10 as a guide. The smoothening step is done subsequently at normal incidence while monitoring the GISAXS intensity. Following the approach described in section 4, the satellite peak intensity will evolve according to

$$I(q,t) \propto \langle |h(q,t)|^2 \rangle - |h(q,\infty)|^2 = (|h(q,0)|^2 - |h(q,\infty)|^2)\mathrm{e}^{-2b(q)t}, \tag{9a}$$

$$|h(q,\infty)|^2 = \frac{v_0 \Omega}{2b(q)}, \tag{9b}$$

$$b(q) = \nu q^2 + K q^4. \tag{9c}$$

The characteristic function $b(q)$ is assumed to be isotropic, because the smoothening step is done with normal incidence ion bombardment. The expressions above actually suggest two possible ways to measure $b(q)$: (i) observe the transient behavior in real time and obtain $b(q)$ from the decay rate, as suggested by equation (9*a*) and (ii) measure the steady-state roughness spectrum given by equation (9*b*), which can be determined through analysis of AFM images of ion

bombardment smoothened surfaces. In this section, data for both approaches are examined.

6.1. Diamond

Datta *et al* have found that a smooth region exists near normal incidence for 10–50 keV Ga^+ bombardment of diamond surfaces, while ripples are formed for angles of incidence above ≈40°. Mayer *et al* have also studied the formation of ripples on diamond at 20 keV and angles of incidence between 40° and 70° [4]. They have shown that the surface can be smoothened at normal incidence after ion bombardment to a fluence of 1.9×10^{18} cm^{-2}. The AFM measurements of Mayer *et al* show that the root-mean-square roughness of an initially roughened surface is reduced from 7.6 to 2.0 nm during normal incidence erosion. The power spectrum from AFM exhibits a q^{-2} behavior at low q and a q^{-1} behavior at high q. The q^{-2} part was suggested to be due to the impact-induced lateral current mechanism, while the q^{-1} part was close to the noise in the measurement. Although in a linear theory the q^{-1} dependence might be interpreted as evidence that bulk viscous flow is a dominant relaxation mechanism, it should be pointed out that the q^{-1} mechanism would dominate over the q^{-2} at *low* q rather than at high q as observed in the experiment. Therefore, the explanation of noise in the AFM image appears to be the more convincing idea.

6.2. Sapphire

6.2.1. GISAXS during smoothening. Figure 11 shows the GISAXS peak intensity during normal incidence ion bombardment of sapphire at $\epsilon = 300$ eV. Each curve corresponds to a different sample, where the ripple wavelength was selected by choosing a specific ion incidence angle between ≈35° and 55°. The data clearly shows the predicted exponential decrease in the satellite peak intensity. The inset shows the relaxation factor $\Lambda(q) = 2b(q)/J_{\text{ion}}$ as a function of the ripple wavenumber q; a clear q^2 dependence is observed. A detailed fit to the Λ versus q data in order to obtain both the K and ν coefficients in $b(q)$ yields a ratio for K/ν of 0.19. In other words, multiple smoothening mechanisms are apparently operative, with the q^2 mechanism being dominant for normal incidence smoothening at small q (long wavelength) and the q^4 mechanism being dominant at large q (short wavelength) The impact-induced lateral current mechanisms described in section 4.3.3 is suggested as the q^2-dependent physical mechanism, since it is the only q^2-dependent mechanism listed in table 1.

6.2.2. Power spectral density of a smoothened surface. The power spectral density (PSD) of a surface is given by $|h(q_x, q_y)|^2/(L_x L_y)$, and is related to magnitude squared of the Fourier transform of the surface height $h(x, y)$ [50]. It can also be integrated to get the root-mean-square surface roughness σ_s:

$$\sigma_s^2 = \frac{1}{(2\pi)^2 L_x L_y} \int |h(q_x, q_y)|^2 \, \mathrm{d}q_x \, \mathrm{d}q_y. \tag{10}$$

If the surface is isotropic, then a circular averaging can be performed without loss of information, so that

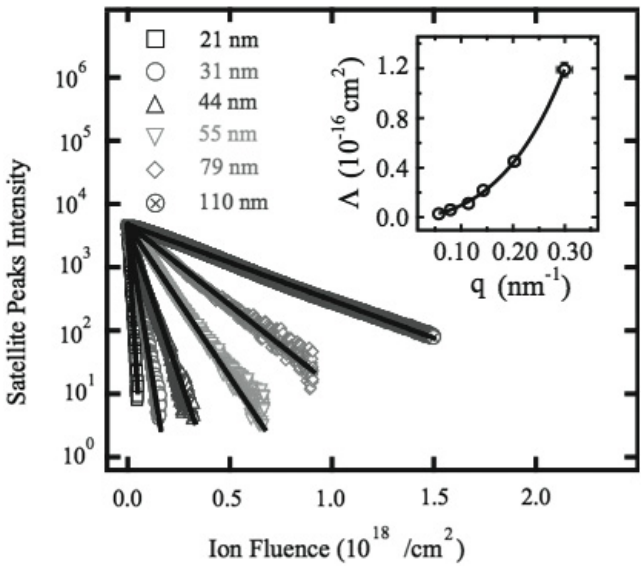

Figure 11. Satellite intensity vs ion fluence for smoothening of ripples of different wavelengths with 300 eV Ar^+. The inset shows the q dependence of the smoothening rate. Reprinted with permission from [3]. Copyright 2008 by the American Physical Society.

$h(q_x, q_y) \to h(q)$, where $q = (q_x^2 + q_y^2)^{1/2}$, and the integral becomes

$$\sigma_s^2 = \frac{1}{2\pi L_x L_y} \int_0^\infty |h(q)|^2 q \, \mathrm{d}q. \tag{11}$$

In atomic force microscopy (AFM), one measures the height of a surface as a function of position to obtain an array $h_{\text{AFM}}(n_x, n_y)$ which approximates the surface profile. The discrete power spectral density (PSD) is directly obtained from the data:

$$h_{\text{AFM}}(q_x, q_y) = \left(\frac{L}{N}\right)^2 \sum_{n_x=0}^{N-1} \sum_{n_y=0}^{N-1} h_{\text{AFM}}(n_x, n_y) \times \exp\left[\mathrm{i}L(q_x n_x + q_y n_y)/N\right], \tag{12a}$$

$$\text{PSD}(q_x, q_y) = \frac{|h_{\text{AFM}}(q_x, q_y)|^2}{L^2}, \tag{12b}$$

where $N_x = N_y = N$ and $L_x = L_y = L$ correspond to the number of samples and the image size in each direction. If the surface is isotropic, then $\text{PSD}(q_x, q_y)$ can be circularly averaged to obtain $\text{PSD}(q)$. Note that many authors plot the PSD as a function of the wavenumber $k = q/2\pi$ so that $2\pi k$ would be substituted into equation (12*a*) in place of q. However, we use q in order to be consistent with the convention used in x-ray scattering. Equations (10) and (11) also reflect this convention.

Figure 12 shows $\text{PSD}(q_x, q_y)$ for smoothened sapphire. The AFM data used to make this figure is shown in figure 3(c). This surface was initially patterned by off-normal ion bombardment and then smoothened at normal incidence until a near steady-state roughness configuration was obtained.

Figure 12 does not exhibit the expected circular symmetry due to the appearance of prominent vertical and horizontal streaks. This is because the noise in the spectrum becomes significant when the surface roughness is low (the rms

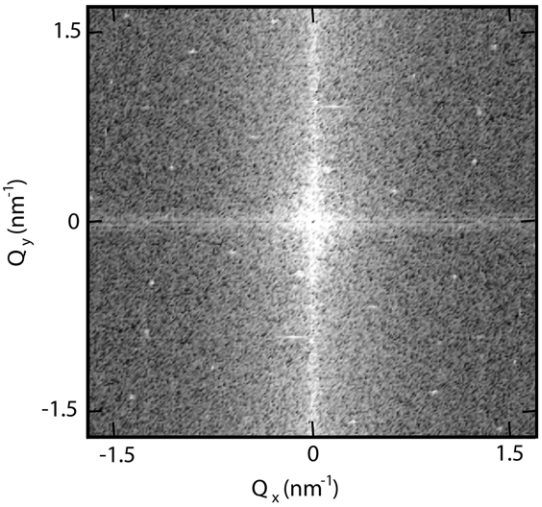

Figure 12. Power spectral density of ion-smoothened sapphire from an atomic force microscope image. The horizontal direction corresponds to the Fourier transform along the fast scanning direction of the microscope stage, while the vertical direction is the slow scanning direction. The vertical and horizontal streaks are related to correlated noise in the image, as discussed in the text. The intensity is displayed on a linear grayscale.

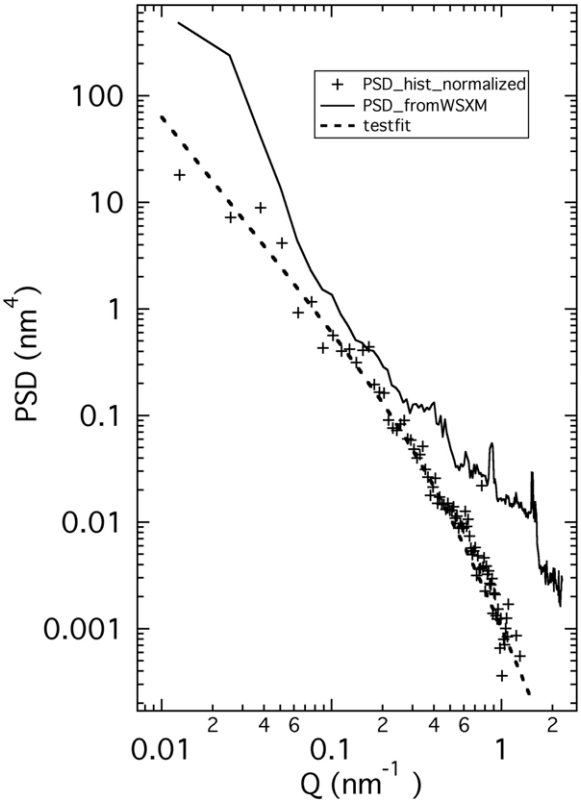

Figure 13. Circularly averaged PSD for ion-smoothened sapphire. The solid line is the PSD for the raw data without any flattening or noise subtraction, while the '+' symbols include subtraction of instrument noise, as described in the text. The dashed line is for the model derived from the GISAXS data with $K/\nu = 0.19$. The noise subtraction changes the root-mean-square roughness derived from the integral of the curve from 0.2 to 0.1 nm.

roughness is ≈0.1 nm in this case). In order to remove this noise, we follow a strategy in which we divide the noise into correlated and uncorrelated components. There are least three sources of correlated noise: (i) hysteresis and creep of the piezo-stage of the AFM causes subsequent scan lines to be displaced, which leads to the vertical streak near $q_x = 0$ in figure 12, (ii) correlated bowing along each scan line leads to the horizontal streak and (iii) noise from vibrations, which appear as sharp peaks in the spectrum. Because all of these correlated noise sources are compact along at least one direction, they can be readily subtracted from the PSD before the circular averaging step. This is done by simply dropping the affected data points from the average. Note that 'flattening' algorithms that operate on the original image data attempt to remove artifacts (i) and (ii) and they are somewhat effective at low q, but are generally not effective at removing the noise at the high-q end of the spectrum. For example, we have attempted background subtraction using the flattening function in the program WSxM [51], and have found that it only removes a small portion of the correlated noise.

Figure 13 shows the azimuthally averaged PSD from the two-dimensional PSD shown in figure 12. The solid line is the circularly averaged PSD without background subtraction. In order to produce the noise-corrected curve, the correlated component of noise was first removed, as described above. The probe tip radius is $R \approx 5$ nm, so the PSD must be dominated by noise above $q = 2\pi/R \approx 1$ nm^{-1}. The uncorrelated noise is taken to be at this level, and was therefore subtracted from the data. The data after removal of correlated noise, subtraction of uncorrelated noise and after the circular averaging step is shown as the '+' symbols in figure 13. We can also compare this data to the theoretical curve with $K/\nu = 0.19$, which is derived from the dynamic smoothening experiment described in the previous section (see figure 11). It is notable that the slope of the theoretical curve increases at high q and that this behavior is reproduced in the background-subtracted PSD, but not in the unmodified PSD where both correlated and uncorrelated noise dominate the spectrum. Therefore, there is no discrepancy between GISAXS and AFM measurements once the noise effects are taken into account.

7. Refined model

As discussed above, the results of surface smoothening experiments clearly show that an additional non-thermal mechanism with q^2 character dominates the surface relaxation in the stable region near normal incidence. The theoretical curve shown in figure 7 can be extended by the addition of a new term ν_{ILC}, which is plotted in figure 8. The new expressions for the ν coefficients are

$$\nu_{\mathrm{eff},x} = \nu_x + \nu_{\mathrm{ILC},x}, \tag{13a}$$

$$\nu_{\mathrm{eff},y} = \nu_y + \nu_{\mathrm{ILC},y}. \tag{13b}$$

This improved model is shown in figure 14. It is seen that the effect of ν_{ILC} is to push the ν terms from negative (destabilizing) to positive (stabilizing). The effect on the ripple phase diagram is dramatic. This relatively simple extension of

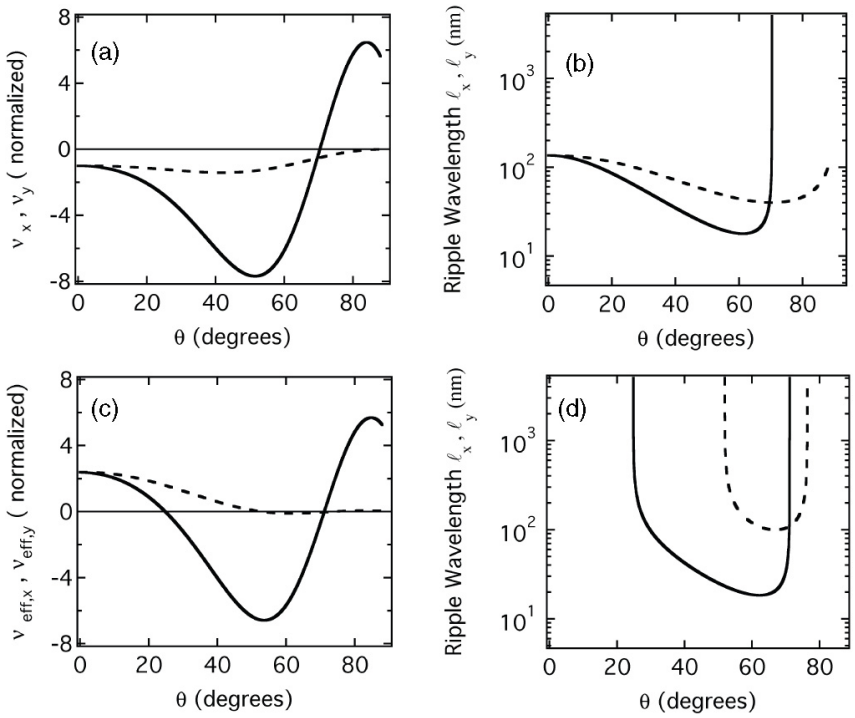

Figure 14. Effect of ν_{ILC} on the ν coefficients and on the ripple wavelength. Parts (a) and (b) correspond to the model before adding the ILC term, while (c) and (d) include the ILC term. The parameters used for the calculation of the erosion instability term are $a = 1.6$ nm, $\mu = 0.5$ nm and $\sigma = 0.4$ nm, which provide a reasonable match to the data for Ar^+ ion bombardment of sapphire at 600 eV. The solid lines correspond to the x direction while the dashed lines correspond to the y direction.

the theory completely explains the incidence angle dependence of the data shown in figure 14.

8. Conclusions

GISAXS has been used in combination with AFM to show that the surface-confined viscous flow mechanism is a dominant smoothening mechanism during low-temperature ripple formation on SiO_2 and sapphire. At high temperature, a type of ion-enhanced surface diffusion becomes the dominant surface relaxation mechanism. A real-time GISAXS measurement shows that the impact-induced lateral current mechanism provides the best explanation of the smoothening effects observed for near-normal incidence. In this paper, it has been shown that the power spectral density derived from AFM measurements of a smoothened sapphire surface are consistent with the GISAXS results if measurement noise is taken into account. Similar observations of q^{-2} behavior found in the literature for AFM scans of ion-smoothened diamond strongly implies that the impact-induced lateral current mechanism is also dominant for other ion–material combinations. The extended BH model is thus found to be in substantial agreement with experimental observations. It is remarkable that the BH theory has continued to be so successful, 20 years after it was first proposed.

Acknowledgments

We would like to acknowledge our collaborators and co-authors on recent papers who contributed to the studies of ripple formation on insulating surfaces, including: Kee-Chul Chang, Karl Ludwig, Gozde Özaydin, Ahmet Özcan, Kit Umbach, Yiyi Wang, Yiping Wang and Lan Zou. The authors acknowledge the experimental assistance of Lin Yang, Christie Nelson, D Peter Siddons, Jie Yang and Vladimir Butko. This material is based upon work supported by the National Science Foundation CAREER program under grant no. DMR-0348354 and by the Department of Energy EPSCoR program under grant no. DE-FG02-03ER46032. National Science Foundation equipment grant DMR-0216704 supported the instrumentation used at the National Synchrotron Light Source X21 beamline. The Cornell High Energy Synchrotron Source is funded by the National Institutes of Health through grant 5P41RR01646-24 and by the National Science Foundation grant DMR-0225180. Use of the National Synchrotron Light Source, Brookhaven National Laboratory, was supported by the US Department of Energy, Office of Science, Office of Basic Energy Sciences, under contract no. DE-AC02-98CH10886.

References

[1] Umbach C C, Headrick R L and Chang K C 2001 *Phys. Rev. Lett.* **87** 246104
[2] Zhou H, Wang Y P, Zhou L, Headrick R L, Özcan A S, Wang Y Y, Özaydin G, Ludwig K F Jr and Siddons D P 2007 *Phys. Rev.* B **75** 155416
[3] Zhou H, Zhou L, Headrick R L, Özaydin G and Ludwig K F Jr 2008 *Phys. Rev.* B **78** 165404
[4] Mayer T M, Adams D P, Vasile M J and Archuleta K M 2005 *J. Vac. Sci. Technol.* A **23** 1579
[5] Ziberi B, Frost F and Rauschenbach B 2006 *J. Vac. Sci. Technol.* A **24** 1344

[6] Mayer T M, Chason E and Howard A J 1994 *J. Appl. Phys.* **76** 1633
[7] Mayr S G and Averback R S 2001 *Phys. Rev. Lett.* **87** 196106
[8] Facsko S, Dekorsy T, Koerdt C, Trappe C, Kurz H, Vogt A and Hartnagel H L 1999 *Science* **285** 1551
[9] Gautier M, Duraud J P, Van L P and Guittet M J 1991 *Surf. Sci.* **250** 71
[10] Özaydin G, Özcan A, Wang Y Y, Ludwig K F Jr, Zhou H, Headrick R L and Siddons D P 2005 *Appl. Phys. Lett.* **87** 163104
[11] Özaydin G, Ludwig K F Jr, Zhou H and Headrick R L 2008 *J. Vac. Sci. Technol.* B **26** 551
[12] Frost F, Fechner R, Ziberi B, Flamm D and Schindler A 2004 *Thin Solid Films* **459** 100
[13] Sigmund P 1969 *Phys. Rev.* **184** 383
[14] Bradley R M and Harper J M E 1988 *J. Vac. Sci. Technol.* A **6** 2390
[15] Sinha S, Sirota E, Garoff S and Stanley H 1988 *Phys. Rev.* B **38** 2297
[16] Rauscher M, Salditt T and Spohn H 1995 *Phys. Rev.* B **52** 16855
[17] Asadchikov V, Kozhevnikov I, Krivonosov Y, Mercier R, Metzger T, Morawe C and Ziegler E 2004 *Nucl. Instrum. Methods Phys. Res.* A **530** 575
[18] Kozhevnikov I and Pyatakhin M 2000 *J. X-Ray Sci. Technol.* **8** 253
[19] Levine J, Cohen J, Chung Y and Georgopoulos P 1989 *J. Appl. Crystallogr.* **22** 528
[20] Eisenberger P and Marra W 1981 *Phys. Rev. Lett.* **46** 1081
[21] Feidenhans'l R 1989 *Surf. Sci. Rep.* **10** 105
[22] Robinson I and Tweet D 1992 *Rep. Prog. Phys.* **55** 599
[23] Dosch H, Batterman B and Wack D 1986 *Phys. Rev. Lett.* **56** 1144
[24] Dosch H 1992 *Int. J. Mod. Phys.* B **6** 2773
[25] Vlieg E, Denier van der Gon A, van der Veen J, Macdonald J and Norris C 1988 *Phys. Rev. Lett.* **61** 2241
[26] Botez C, Miceli P and Stephens P 2001 *Phys. Rev.* B **64** 125427
[27] Malis O, Brock J, Headrick R, Yi Min-Su and Pomeroy J 2002 *Phys. Rev.* B **66** 035408
[28] Peverini L, Ziegler E, Bigault T and Kozhevnikov I 2007 *Phys. Rev.* B **76** 045411
[29] Peverini L, Ziegler E and Kozhevnikov I 2007 *Appl. Phys. Lett.* **91** 053121
[30] Sánchez-García J A, Vázquez L, Gago R, Redondo-Cubero A, Albella J M and Czigány Z 2008 *Nanotechnology* **19** 355306
[31] Ziberi B, Frost F, Tartz M, Neumann H and Rauschenbach B 2004 *Thin Solid Films* **459** 106
[32] Zhou H and Headrick R L 2007 unpublished
[33] Ziegler J F, Biersack J P and Littmark U 1985 *Stopping and Range of Ions in Solids* (New York: Pergamon)
[34] Makeev M A, Cuerno R and Barabási A L 2002 *Nucl. Instrum. Methods Phys. Res.* B **197** 185
[35] Stearns D 1993 *Appl. Phys. Lett.* **62** 1745
[36] Pimpinelli A and Villain J 1999 *Physics of Crystal Growth* (Cambridge: Cambridge University Press)
[37] Mullins W 1959 *J. Appl. Phys.* **30** 77
[38] Herring C 1950 *J. Appl. Phys.* **21** 301
[39] Orchard S E 1962 *Appl. Sci. Res.* A **11** 451
[40] Cuerno R and Barabási A-L 1995 *Phys. Rev. Lett.* **74** 4746
[41] Asaro R and Tiller W 1972 *Metall. Trans.* **3** 1789
[42] Carter G and Vishnyakov V 1996 *Phys. Rev.* B **54** 17647
[43] Facsko S, Bobek T, Stahl A and Kurz H 2004 *Phys. Rev.* B **69** 153412
[44] Davidovich B, Aziz M and Brenner M 2007 *Phys. Rev.* B **76** 205420
[45] Moseler M, Gumbsch P, Carsiraghi C, Ferrari A C and Lieb J R 2005 *Science* **309** 1545
[46] Park S, Kahng B, Jeong H and Barabási A-L 1999 *Phys. Rev. Lett.* **83** 3486
[47] Zhou H 2007 *PhD Thesis* University of Vermont, Burlington, Vermont
[48] Datta D, Wu Y-R and Wang Y 2001 *Phys. Rev.* B **63** 125407
[49] Vajo J J, Doty R E and Cirlin E H 1996 *J. Vac. Sci. Technol.* A **14** 2709
[50] Stover J 1995 *Optical Scattering: Measurement and Analysis* 2nd edn (Bellingham, WA: SPIE Optical Engineering Press)
[51] Horcas I, Fernández R, Gómez-Rodríguez M, Colchero J, Gómez-Herrero J and Baro A 2007 *Rev. Sci. Instrum.* **78** 013705